Spectroscopic study of $^{10}_{\Lambda}$B, $^{12}_{\Lambda}$C, $^{28}_{\Lambda}$Si, $^{89}_{\Lambda}$Y, $^{139}_{\Lambda}$La, and $^{208}_{\Lambda}$Pb by the (π^+,K^+) reaction

T. Hasegawa,* O. Hashimoto,† S. Homma, T. Miyachi, T. Nagae, M. Sekimoto, and T. Shibata
Institute for Nuclear Study, University of Tokyo, Tanashi, Tokyo 188, Japan

H. Sakaguchi and T. Takahashi
Department of Physics, Kyoto University, Kitashirakawa, Sakyo-ku, Kyoto 606, Japan

K. Aoki and H. Noumi
National Laboratory for High Energy Physics (KEK), Oho, Tsukuba, Ibaraki 305, Japan

H. Bhang and M. Youn
Department of Physics, Seoul National University, Seoul 151-742, Korea

Y. Gavrilov
Institute for Nuclear Research, Academy of Science, 117312 Moscow, Russia

S. Ajimura, T. Kishimoto, and A. Ohkusu
Department of Physics, Osaka University, Toyonaka, Osaka 660, Japan

K. Maeda
Department of Physics, Tohoku University, Aoba-ku, Sendai, Miyagi 980-77, Japan

R. Sawafta
Physics Department, Brookhaven National Laboratory, Upton, New York 11973

R. P. Redwine
Laboratory for Nuclear Science, Massachusetts Institute of Technology, Cambridge, Massachusetts 02139
(Received 6 July 1995)

Hypernuclear mass spectra of $^{10}_{\Lambda}$B, $^{12}_{\Lambda}$C, $^{28}_{\Lambda}$Si, $^{89}_{\Lambda}$Y, $^{139}_{\Lambda}$La, and $^{208}_{\Lambda}$Pb were measured by the (π^+,K^+) reaction with an energy resolution of 2 MeV (FWHM). The experiment was carried out with a 1.06 GeV/c π^+ beam from the KEK 12-GeV PS and with the superconducting kaon spectrometer (SKS). For light hypernuclei, core-excited states were resolved for the first time. For heavy hypernuclei, peak structure reflecting Λ shell structure was observed.

PACS number(s): 21.80.+a, 25.80.Hp

I. INTRODUCTION

Since the first discovery in 1952 in emulsion [1], various Λ hypernuclei have been observed. In particular, after an experiment employing counter techniques at CERN in 1973 [2], many counter experiments have been carried out with the (K^-,π^-) and the (stopped K^-,π^-) reaction at CERN, BNL [3–7], and KEK [8–10]. In spite of such a long history, the existing experimental data are limited mostly to light hypernuclei. In order to understand the behavior of a Λ hyperon in a nucleus, systematic experimental data over the whole mass-number range, especially of heavy hypernuclear bound states, have been long awaited.

The (π^+,K^+) reaction was proposed to be effective tool for spectroscopic study of heavy hypernuclei by Thiessen [11] and Dover *et al.* in 1980 [12]. Intensive theoretical studies followed [13,14]. The usefulness of the reaction was demonstrated experimentally at BNL [15–17] and at KEK [18]. Various bound states were resolved, from $^{9}_{\Lambda}$Be to $^{89}_{\Lambda}$Y. The observed spectra exhibited characteristic peak structure reflecting Λ shell structure. It was argued that the results were consistent with the independent single-particle picture of Λ hypernuclei.

The (π^+,K^+) reaction is characterized by large momentum transfer, as much as 0.35 GeV/c, which is comparable to the Fermi momentum. Owing to this large momentum transfer, it preferentially populates angular-momentum stretched states with the largest l neutron-hole configurations. Furthermore, the reaction mechanism is simpler because of the higher pion momentum of about 1 GeV/c, at which the elementary cross section of a Λ hyperon takes a sharp maximum. In addition, highly excited states of heavy hypernuclei are expected to have quite narrow widths [14,19,20]. This situation is in contrast with the nucleon case, in which deep-hole states are too broad to be observed as well-defined peaks. Because of these features, characteristic peaks reflect-

*Present address: School of Allied Health Sciences, Kitasato University, Kitasato 1-15-1, Sagamihara-shi, Kanagawa 228, Japan.
†Present address: Department of Physics, Tohoku University, Aoba-ku, Sendai, Miyagi 980-77, Japan.

ing Λ shell structure are expected to be resolved even for heavy hypernuclei such as $^{208}_{\Lambda}$Pb, if one has a good energy resolution. In particular, deeply bound single-particle states can be observed as peaks.

Precise spectroscopic data of Λ hypernuclei give us important information about the ΛN interaction. In this respect, *p*-shell hypernuclei have been studied by configuration mixing shell models [21–24]. A complementary role of the (π^+,K^+) reaction should be emphasized. The (π^+,K^+) reaction selectively populates angular-momentum stretched states for all of the Λ orbits. On the other hand, the (K^-,π^-) reaction favors substitutional states, owing to its small momentum transfer. The (stopped K^-,π^-) reaction also has a sizable momentum transfer, but is not so selective as the (π^+,K^+) reaction because of angular momentum coupling of a K^--atom and larger distortion [13]. Therefore, even for light hypernuclei, the (π^+,K^+) method is useful for extracting new spectroscopic information. Good energy resolution is indispensable also in this case in order to resolve fine structure reflecting the residual ΛN interaction.

The present paper reports a systematic and precise spectroscopic study of Λ hypernuclei over a mass-number range up to 208 with an energy resolution of 2 MeV [full width at half maximum (FWHM)]. In particular, this is the first attempt to observe directly deeply bound single-particle states of such heavy hypernuclei. With the good energy resolution, new fine structures of core-excited states are expected to be resolved for light hypernuclei.

II. APPARATUS

A. Outline

The experiment used a 1.06 GeV/*c* π^+ beam at the K6 beam line of the KEK 12-GeV PS. Incident pions and scattered kaons were detected by two independent spectrometers: a beam line spectrometer and the superconducting kaon spectrometer (SKS) [25–28]. Details of the present system are described elsewhere [29]. The good energy resolution was the most essential specification to resolve Λ shell structure of heavy hypernuclei and core-excited states of light hypernuclei. In order to achieve the resolution, the two spectrometers were designed to have a momentum resolution of 0.1% (FWHM) in a momentum range around 1 GeV/*c*. Simultaneously, the kaon spectrometer kept a large angular acceptance and a short flight path with a powerful kaon trigger system.

B. K6 beam line

The K6 beam line is a separated secondary-particle beam line in the 1-GeV/*c* momentum range [30]. The primary proton beam was extracted from the KEK 12-GeV PS for 1.4 sec in each 4.0 sec to a platinum pion production target. The beam line had a dc separator, which was operated at ±200 kV for π^+/p separation. The p/π^+ and e^+/π^+ ratios were measured to be typically 10 and 20%, respectively. The central beam momentum was set at 1.06 GeV/*c*. The beam intensity was adjusted to be about 3 M/spill. The beam size was measured to be typically 6.0(H) × 7.5(V) mm^2 in rms at the experimental target.

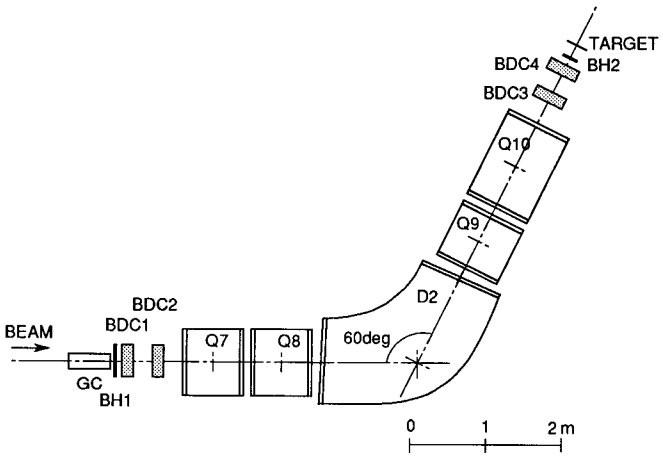

FIG. 1. Schematic view of the beam line spectrometer.

C. Beam line spectrometer

The last part of the K6 beam line is the beam line spectrometer (Fig. 1). It comprises a *QQDQQ* magnet system, three trigger counters (BH1, BH2, and GC), and four sets of drift chambers (BDC1∼4).

The beam hodoscope (BH1), with seven vertical segments, was used as the time-zero counter. A coincidence of BH1 with BH2 rejected not only proton contamination in the beam, but also background particles which could not pass through the magnets. The single counting rate of BH1 was about twice of that of BH2. Since BH2 was placed between the two spectrometers, it was made thin (2 mm) to minimize the energy-loss straggling. The gas Čerenkov counter (GC) vetoed positron contamination in the beam with a rejection efficiency of better than 99.9%.

Each set of the drift chambers comprised six anode planes (*xx′*, *uu′* and *vv′*: *xx′* vertical wires: *uu′* and *vv′* ±15° tilted). In order to minimize the multiple-scattering effect on the momentum resolution, the $(x|\theta)$ term of the transfer ma-

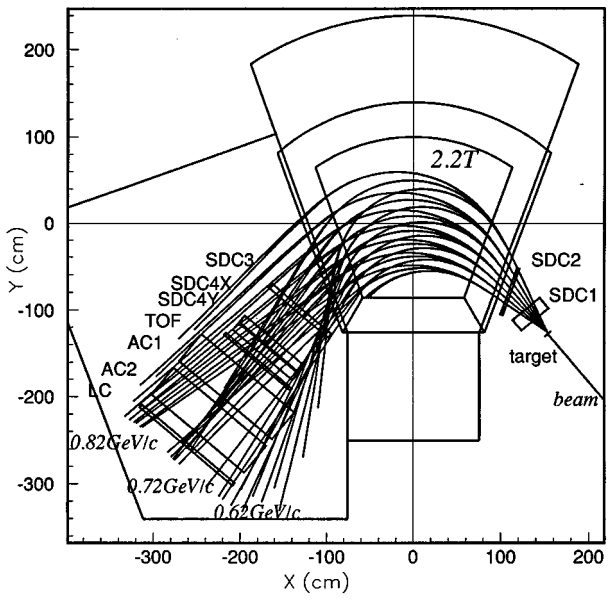

FIG. 2. Schematic top view of SKS.

TABLE I. Data acquisition schedule. The integrated BEAM count is denoted by N_{BEAM}.

Cycles	Targets	N_{BEAM}
92-11	^{12}C	30.1 G
	^{28}Si	147.9 G
	^{89}Y	254.5 G
92-12	^{12}C	58.5 G
	^{139}La	513.2 G
93-02	^{12}C	76.8 G
	^{208}Pb	113.7 G
93-03	^{12}C	83.3 G
	^{208}Pb	571.3 G
93-04	^{12}C	70.9 G
	^{10}B	145.0 G
	^{208}Pb	168.7 G

trix between BDC2 and BDC3 was set to be zero to the first order. In addition, a vacuum chamber was installed between BDC2 and BDC3 through the magnets. A Monte Carlo simulation shows that the expected resolution is 0.04% (FWHM). The fluctuation of the D2 magnetic field was monitored with a high-precision Hall probe and found to be within $\pm 0.05\%$.

D. The superconducting kaon spectrometer (SKS)

Figure 2 shows a schematic view of the SKS. A special characteristic feature is compatibility of a good momentum resolution of 0.1% (FWHM) with a large angular acceptance of 100 msr in the 1-GeV/c momentum range. The spectrometer comprises a sector-shape superconducting dipole magnet with five sets of drift chambers (SDC1, SDC2, SDC3, SDC4X, and SDC4Y) for momentum measurement and three kinds of trigger counters (TOF, AC1, AC2, and LC) for particle identification.

The drift-cell structure of SDC1$\cdot$2 was the same as that of BDC's. The SDC4X$\cdot$Y had a special wire configuration where each cell had six sense wires staggered by ± 200 μm in order to solve left-right ambiguities. The TOF wall comprised fifteen vertical scintillation counters. The LC wall comprised fourteen vertical threshold-type Lucite Čerenkov counters, which discriminated protons from pions and kaons. The AC1 and AC2 [31] are threshold-type Čerenkov counters with silica aerogel as the radiators for pion veto. The refractive index was about 1.06. The efficiency of one layer was about 99% for 0.72 GeV/c pions. In order to avoid deterioration of the transparency of the silica aerogel due to moisture, nitrogen gas was flowed through the counter boxes.

In the present experiment, the magnet was operated at the 2.2 T mode, where the central trajectory corresponded to 0.72 GeV/c. Helium bags were installed between SDC1 and SDC4X to avoid multiple scattering by air. Monte Carlo simulation showed that the precision of the magnetic field map was the most important factor which limited the momentum resolution. Therefore, the magnetic field distribution was measured over the entire spectrometer volume with Hall probes prior to the data acquisition. The magnetic field was monitored with an NMR probe during the data acquisition and found to be stable.

TABLE II. Specifications of the experimental targets.

Targets	Thickness (g/cm^2)	Abundance (%)
^{12}C	0.89 ± 0.03	98.9 (natural)
^{10}B	2.14 ± 0.05	99 (enriched)
^{28}Si	2.37 ± 0.05	92.2 (natural)
^{89}Y	3.13 ± 0.04	100.0 (natural)
^{139}La	3.66 ± 0.04	99.9 (natural)
^{208}Pb	3.41 ± 0.17	99 (enriched)

E. Trigger and data acquisition

The (π^+,K^+) trigger was defined by BEAM $\times$ TOF $\times$ $\overline{\mathrm{AC1}}$ $\times$ $\overline{\mathrm{AC2}}$ $\times$ LC, where BEAM was defined by BH1 $\times$ BH2 $\times\overline{\mathrm{GC}}$. The trigger timing was determined by BH1. The trigger rate was typically 400 counts/spill for a pion beam rate of 3 M/spill. Most of these events were related to background pions and protons.

The raw signals were digitized by TDC and ADC modules of the KEK-TKO standard [32]. The digitized data were transferred into memory modules in a VME crate event by event. During a spill-off period of 2.6 sec, those accumulated data were recorded on an 8 mm tape after being processed by a VME CPU (68020) module. A typical data size was 150 words per event. A typical dead time was 8% for a trigger rate of 400 counts/spill.

Table I shows a data-acquisition schedule. The data were taken in five separated accelerator-operation-cycles from February to July in 1993. In each cycle, ^{12}C(π^+,K^+) data were taken for calibration.

Table II shows specifications of the targets. The thickness was chosen so as to make the energy-loss straggling sufficiently small to keep the energy resolution of about 2 MeV.

III. DATA ANALYSIS

A. Outline

The hypernuclear mass (M_{HY}) was calculated by a kinematical relation,

$$M_{HY}=\sqrt{(E_\pi+M_A-E_K)^2-(p_\pi^2+p_K^2-2p_\pi p_K\cos\theta)}, \tag{1}$$

where M_A is the target nuclear mass; θ is the scattering angle; p_π and E_π (p_K and E_K) are the momentum and energy of pions (kaons), respectively. Thus there were three kinematical variables to be measured. The data reduction proceeded as follows: (1) rough event selection, (2) track reconstruction and momentum determination for pions, (3) track reconstruction and momentum determination for kaons, (4) (π^+,K^+) event selection, and (5) calculation of hypernuclear mass spectra.

B. Rough event selection

The (π^+,K^+) events were selected step by step along the analysis procedures. For precise event selection, the tracking

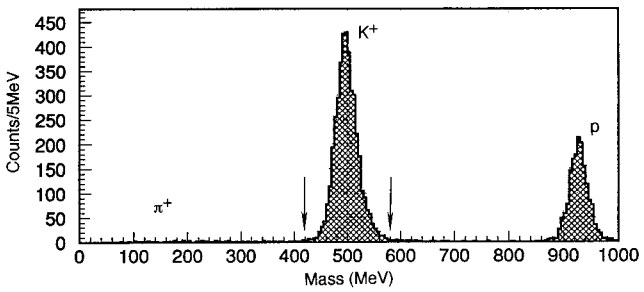

FIG. 3. Scattered particle mass distribution for the $^{12}_{\Lambda}$C data. The selected region is indicated by the arrows.

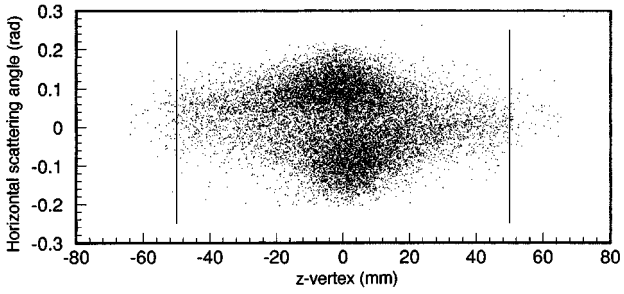

FIG. 4. Scatter plot between the z vertex and the horizontal scattering angle at the target for the 93-02 cycle $^{12}_{\Lambda}$C data.

in the two spectrometers had to be completed. However, the tracking was a time-consuming process. Therefore, before the pion tracking, the analysis program rejected bad events for which some of BDC1.2.3.4 or some of SDC1.2.3.4X.4Y did not have sufficient hit information. In addition, loose cuts were applied to the ADC's of TOF and LC to reject background events. By this rejection, the number of events to be analyzed was reduced by about a factor of 10.

C. Pion tracking

Straight tracks were defined locally at the entrance of $QQDQQ$ with BDC1·2 and at the exit with BDC3·4 by the linear least-squares fitting. For a multihit event, all possible combinations were examined. For each track at the exit, the best track at the entrance was selected by comparing the χ^2 values defined with a third-order transfer matrix calculated by ORBIT [33]. Then, the momentum was obtained. Since the calculated matrix was not sufficiently accurate, the momentum was corrected as follows. The correction terms were calibrated by the SKS by leading a 1.06 GeV/c pion beam through the two spectrometers, where a program [34] based on the principal component analysis [35] was used.

D. Kaon tracking

Straight tracks were defined by SDC1·2. In SDC4X·Y, left-right ambiguity was solved by themselves before tracking. Then, the momentum was calculated by the Runge-Kutta tracking method [36,37] with a measured magnetic field map. The SDC3 data were used to reject background events for which tracks could not be reconstructed. The applied χ^2_i cut was at $\chi^2_i = 16$. After the kaon tracking, the number of the events was reduced to be about one-hundredth of that of the recorded data. Most of these rejected events belonged to the background.

E. (π^+,K^+) event selection

The mass of scattered particles ($M_{\rm scattered}$) was calculated by

$$M_{\rm scattered} = \frac{p}{\beta}\sqrt{1-\beta^2}, \tag{2}$$

where β is the velocity measured by time of flight between BH1 and TOF; p is the momentum calculated in the kaon tracking. Figure 3 shows a typical mass distribution for $^{12}_{\Lambda}$C data, where the selected region is indicated. The π^+ events had been well suppressed owing to the excellent performance of the aerogel Čerenkov counters at the trigger stage.

Figure 4 shows a scatter plot between the z vertex and the horizontal scattering angle at the target, where the selected region is shown by solid lines. Rather tight cuts were required to suppress the background level sufficiently well. The scattering angle was determined from two local straight tracks defined by BDC3·4 and SDC1·2, respectively. Typical scattering angle resolutions were 0.004 and 0.014 rad (rms) in horizontal and vertical, respectively. The vertical resolution was worse than the horizontal one because of the special wire configuration of the drift chambers.

F. Energy calibration

The momentum measurement of pions and kaons suffered from systematic errors in the geometrical parameters of the tracking detectors and in the measured magnetic field map. Therefore, the $^{12}_{\Lambda}$C data were used for the purpose of the energy calibration as follows. The kaon momentum scale was shifted by about -4 MeV/c so as to adjust the $^{12}_{\Lambda}$C ground state peak position at $B_\Lambda = 10.76$ MeV. This value is based on other $^{12}_{\Lambda}$C experiments [6,8,17,18,38,39]. Note that a kaon momentum shift is approximately identical to a pion momentum shift in calculating the hypernuclear mass. The calibration was carried out cycle by cycle independently.

G. Cross section

The cross section was obtained by integrating selected yields over the spectrometer acceptance:

$$\sigma_{2-14^\circ} \equiv \left(\int_{\theta=2^\circ}^{\theta=14^\circ} \frac{d^2\sigma}{dE d\Omega} d\Omega \right) \Delta E_{\rm bin}, \tag{3}$$

where $\Delta E_{\rm bin}$ is a spectrum bin width. The lower limit of θ was set in order to reject background events associated with (π,π) events. The following factors were taken into account in the calculation: detector and analysis efficiency, beam normalization, data-acquisition efficiency, angular acceptance of SKS, K^+ decay effects, K^+ absorption effects, and target thickness.

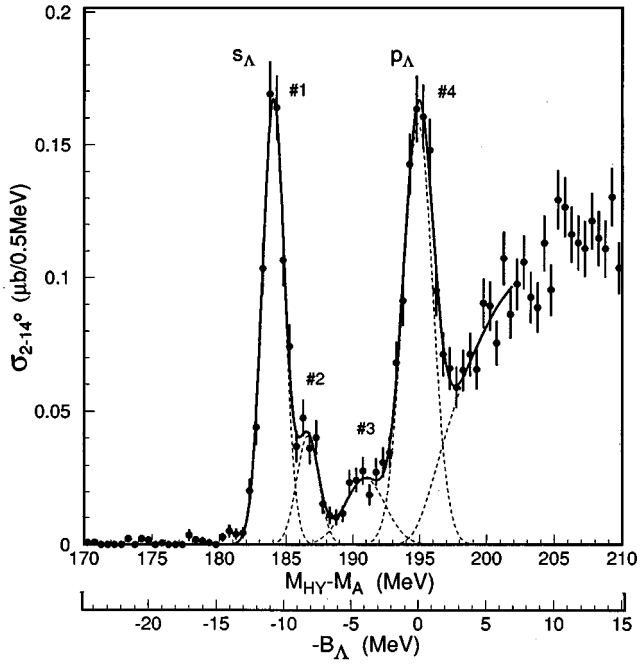

FIG. 5. Hypernuclear mass spectrum of $^{12}_{\Lambda}$C with a fitting curve described in the text.

1. Detector and analysis efficiency

The BDC detector and analysis efficiency was measured run by run with BEAM trigger data mixed with the (π^+,K^+)-trigger data. It was typically $70\pm2\%$ in total, where the error is statistical. The SDC1·2 detector and analysis efficiency was measured in the same way to be $80\pm2\%$. The SDC3·4X·Y detector and analysis efficiency was measured by using a 0.72 GeV/c pion beam. They were

TABLE III. Ground-state cross section of $^{12}_{\Lambda}$C for each experimental cycle with various beam intensities. The quoted errors are statistical.

Cycles	BEAM rate (M/spill)	N_{BEAM}	$\sigma_{2-14°}$ (μb)
92-11	3.4	30.1 G	0.72 ± 0.06
92-12	3.9	58.5 G	0.65 ± 0.04
93-02	2.4	76.8 G	0.61 ± 0.04
93-03	2.9	82.3 G	0.61 ± 0.04
93-04	2.9	70.9 G	0.69 ± 0.04
93-04	1.0	3.7 G	0.73 ± 0.12
93-04	2.1	4.6 G	0.73 ± 0.12
93-04	2.9	3.6 G	0.69 ± 0.12

$98.0\pm1.5\%$ and $94.0\pm1.5\%$ for SDC3 and SDC4X·Y, respectively. The TOF efficiency was measured with a 0.72 GeV/c pion beam to be $99.8\pm0.2\%$. The efficiency was assumed to be the same for kaons because the energy-loss difference was small. The LC efficiency was similarly measured to be $99.8\pm0.2\%$ for pions. The efficiency was estimated to be $99.0\pm1.0\%$ for kaons by a simple Monte Carlo simulation where the pulse height for kaons was typically 40% of that for pions. The tracking efficiency other than the detector analysis efficiency is assumed to be 100% on the basis of a Monte Carlo simulation.

The kaon-tracking-χ^2 cut efficiency and the z-vertex cut efficiency were estimated to be $84\pm2.0\%$ and $90\pm2\%$, respectively, assuming that the background level was approximately uniform over the energy scale. Each of the scattered-particle-mass cut efficiency, the ADC cut efficiency for TOF and that for LC was calculated to be $99.0\pm1.0\%$ by Gaussian fitting.

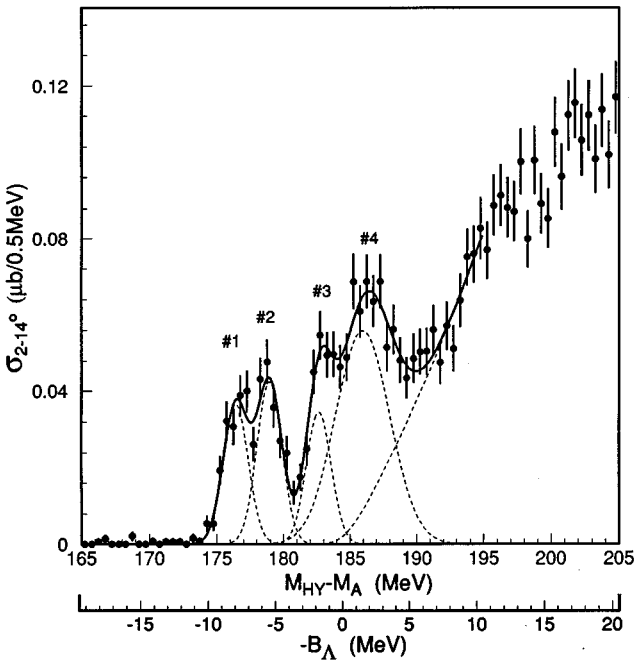

FIG. 6. Hypernuclear mass spectrum of $^{10}_{\Lambda}$B with a fitting curve described in the text.

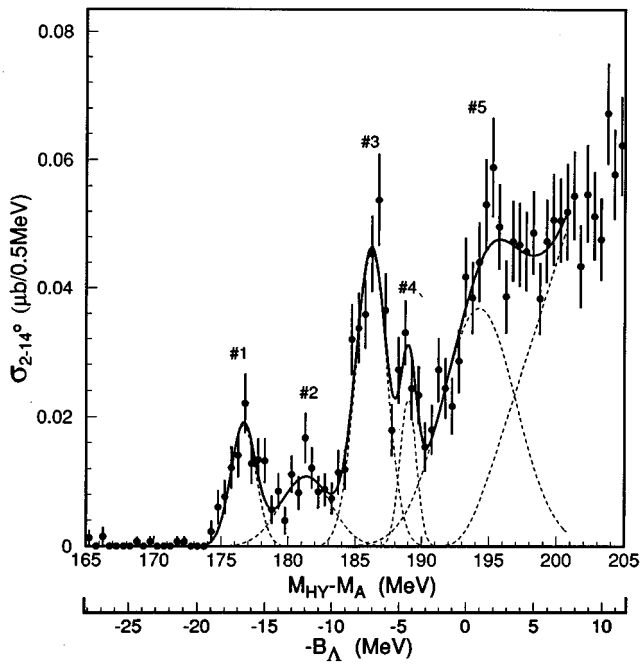

FIG. 7. Hypernuclear mass spectrum of $^{28}_{\Lambda}$Si with a fitting curve described in the text.

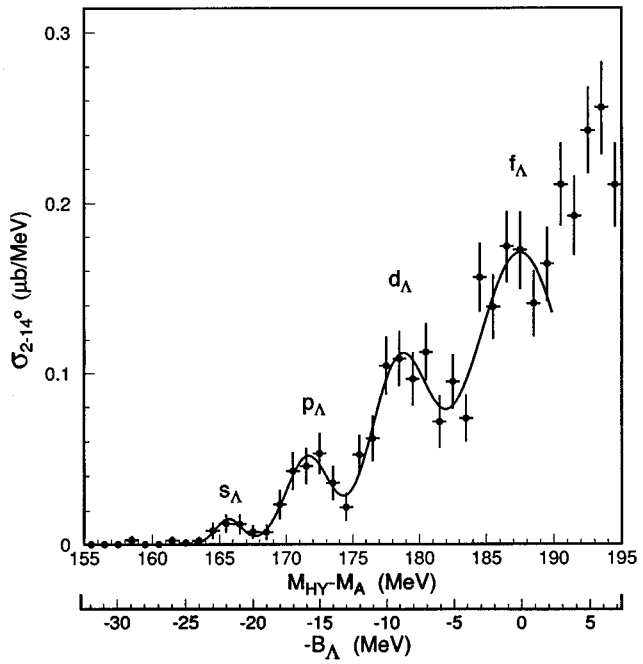

FIG. 8. Hypernuclear mass spectrum of $^{89}_{\Lambda}$Y with a fitting curve described in the text.

2. Beam normalization

The μ^+ contamination at the target was estimated to be 5.9–6.5 % at 1.00–1.10 GeV/c with DECAY TURTLE [40]. Under a different beam-transport condition, the μ^+ contamination was measured directly with an additional high-pressure Freon-gas Čerenkov counter. In this case, a DECAY TURTLE calculation agreed with the measured result within $\pm 1.5\%$. Therefore, we assume that the error is $\pm 2.0\%$ including the momentum dependence. The accidental coincidence rate between BH1 and BH2 was calculated run by run with BEAM trigger data by using TDC spectra to be $3.0 \pm 0.5\%$ in typical. The tails of beam profiles were cut, where the cut efficiency was calculated by Gaussian fitting to be $94.0\% \pm 2.0\%$.

3. Other factors

The data-acquisition efficiency was measured by scalers run by run to be typically $92.0 \pm 0.1\%$. Because of a high counting rate of AC1·2, as high as 1.6 M/spill due to background particles, the accidental veto in the trigger could not be ignored. The corresponding correction factor was calculated from the rate and the coincidence width to be typically $93 \pm 1\%$.

The angular acceptance of SKS was calculated by a Monte Carlo simulation, taking account of the measured beam profile. The maximum integrated solid angle was about 100 msr. The angular range was asymmetric: $\pm 15^\circ$ in horizontal and $\pm 5^\circ$ in vertical.

A Monte-Carlo simulation showed that the kaon decay rate was typically $39.5 \pm 2.0\%$. The momentum dependence was about 0.04%/(MeV/c) and taken into account in the cross section calculation. The scattering angle dependence was found to be small.

The K^+N cross section is dominated by the elastic scattering in the momentum range below 0.8 GeV/c. The inelastic cross section is less than 0.5 mb around 0.7 GeV/c [41]. Therefore, the kaon absorption rate is negligibly small ($<0.4\%$).

4. Total systematic errors

The total systematic error in the cross section was assumed to be the square root of the quadratic sum of all the individual errors described above. In total, they amounted to 15% for $^{12}_{\Lambda}$C, 14% for $^{10}_{\Lambda}$B and $^{28}_{\Lambda}$Si, 13% for $^{89}_{\Lambda}$Y and $^{139}_{\Lambda}$La, and 17% for $^{208}_{\Lambda}$Pb. The error in the target thickness is shown in Table II. The error in the acceptance was assumed to be zero.

The consistency of the cross section calculation was examined by comparing ground-state cross sections of $^{12}_{\Lambda}$C. They were calculated separately for each experimental cycle to check the long term stability, and for various beam intensities to check the beam rate dependence. They are consistent with one another as shown in Table III.

IV. EXPERIMENTAL RESULTS

A. Hypernuclear mass spectra

Obtained hypernuclear mass spectra of $^{10}_{\Lambda}$B, $^{12}_{\Lambda}$C, $^{28}_{\Lambda}$Si, $^{89}_{\Lambda}$Y, $^{139}_{\Lambda}$La and $^{208}_{\Lambda}$Pb are shown in Figs. 5–10 respectively. The vertical scale is the cross section integrated from $\theta = 2^\circ$ to 14°. The horizontal energy scale is given by the mass difference, $M_{HY} - M_A$, and the binding energy, which was calculated by

$$B_\Lambda = \overline{M_{\text{core}}} - M_{HY} + M_\Lambda . \tag{4}$$

For $^{12}_{\Lambda}$C, $^{10}_{\Lambda}$B and $^{28}_{\Lambda}$Si, $\overline{M_{\text{core}}}$ is the mass of the ground state core nucleus. For $^{89}_{\Lambda}$Y, $^{139}_{\Lambda}$La and $^{208}_{\Lambda}$Pb, it was shifted by

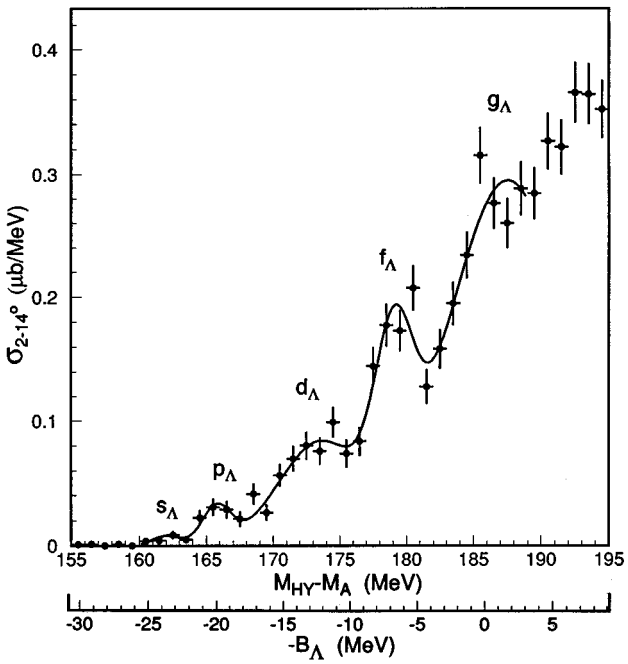

FIG. 9. Hypernuclear mass spectrum of $^{139}_{\Lambda}$La with a fitting curve described in the text.

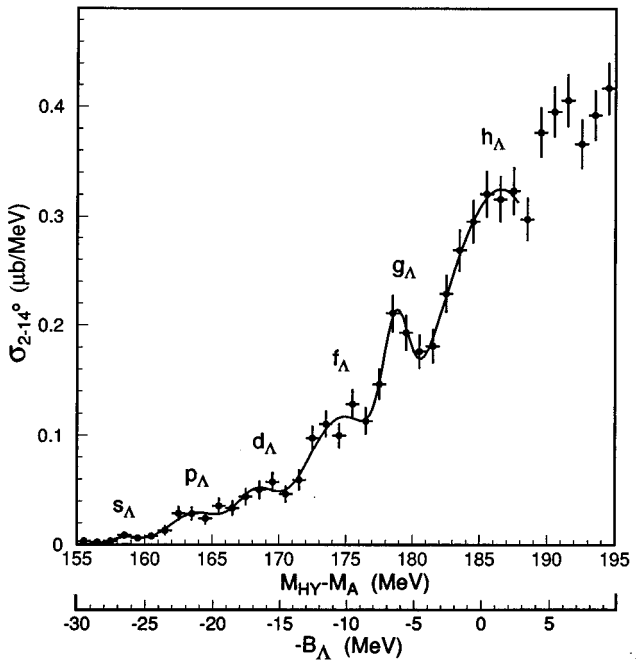

FIG. 10. Hypernuclear mass spectrum of $^{208}_{\Lambda}$Pb with a fitting curve described in the text.

+0.15, +0.99 and +1.63 MeV, respectively, in order to take account of unresolved fragmentation of the neutron hole strength [42].

B. Energy precision

The energy scale was calibrated so as to adjust the $^{12}_{\Lambda}$C ground state peak position as described already. This calibration was performed cycle by cycle with a fitting error of ± 0.3 MeV. The linearity of the SKS momentum scale was examined by sending beams through the two spectrometers at several central beam momenta from 0.65 to 0.82 GeV/c by 2% steps. The linearity was found to be better than 0.1 MeV/c. The linearity of the beam spectrometer is expected to be similar to that of the SKS because it was calibrated with the SKS. (In total, the simple summation of these errors amounts to ± 0.5 MeV.)

C. Energy resolution

The experimental energy resolution was determined by the momentum resolution of the two spectrometers and by the energy-loss fluctuation in the target. The resolution was found to be 1.9 ± 0.1 MeV (FWHM) for the ground-state peak in the case of $^{12}_{\Lambda}$C. For the other targets, the mean-energy-loss and the energy-loss straggling were different. The resolution was calculated with the Bethe-Bloch formula and the Vavilov distribution [43] to be 2.2, 2.2, 2.2, 2.3, and 2.2 ± 0.1 MeV for $^{10}_{\Lambda}$B, $^{28}_{\Lambda}$Si, $^{89}_{\Lambda}$Y, $^{139}_{\Lambda}$La, and $^{208}_{\Lambda}$Pb, respectively.

D. Background level

Figure 11 shows the overbound regions of the $^{12}_{\Lambda}$C, $^{89}_{\Lambda}$Y, $^{139}_{\Lambda}$La, and $^{208}_{\Lambda}$Pb spectra, where no entry is expected ideally. The background yields look uniform in the overbound regions. The background cross section is typically less than 0.006 μb/MeV. No-target (π^+,K^+) data were analyzed with the same analysis program as that for the normal (π^+,K^+) data. The background cross section was found to be less than 0.01 μb/MeV. A Monte Carlo simulation shows that background events associated with kaon decay were well rejected by the tracking in the SKS. On the basis of these results, we assumed that the background level was negligible in peak fitting.

V. DISCUSSION

A. $^{12}_{\Lambda}$C

The $^{12}_{\Lambda}$C spectrum exhibits two prominent peaks at $B_\Lambda = 11$ and 0 MeV and two small peaks between them. The two large peaks were already observed in previous (π^+,K^+) experiments [15–18]. They were interpreted as neutron-hole Λ-particle configurations of $[0p_{3/2}^{-1},s_\Lambda]$ and $[0p_{3/2}^{-1},p_\Lambda]$, respectively. The measured angular distribution was shown to be consistent with the above interpretation [15].

The two small peaks are resolved for the first time, although non-negligible strength between the s_Λ and p_Λ peaks was discussed before [8,17,44]. On the basis of the weak coupling picture, they are related to the excited states of ^{11}C at 2.0 $(1/2^-)$ and 4.8 $(3/2^-)$ MeV with the Λ hyperon in the s_Λ orbit. Theoretically, these core-excited states have been discussed with configuration-mixing shell models in conjunction with the ΛN interaction [21–24].

The spectrum was fitted with four Gaussians and a quasi-free part representing a continuum spectrum in the unbound region. The quasifree part was given by a second-order polynomial starting at $B_\Lambda = 0$ being folded by the energy resolution. The Gaussian widths were set as free parameters in the fitting. The fitting results are shown in Table IV. The excitation energies of the No. 2 and No. 3 peaks are larger than those of the two excited states, possibly reflecting the ΛN interaction.

The present $^{12}_{\Lambda}$C spectrum was already discussed in a separate letter paper in detail [45]. It compared the fitting results with recent theoretical calculations based on a configuration-mixing shell model [23,24]. The calculation showed that the peak positions and intensities were sensitive to the ΛN interaction. Various interaction models, such as the Nijmegen D (ND), F (NF), SC (NSC) and Jülich A (JA), B (JB), were compared. Among these, the NSC potential resulted in relatively larger excitation energies, which are closest to the present experimental results. This may be due to the special character of NSC: a large ratio of spin-singlet to spin-triplet terms. Therefore, the paper claimed that a stronger spin-singlet strength was favored. This conclusion is consistent with the spin-parity assignment of the spin doublet of $^{4}_{\Lambda}$H($^{4}_{\Lambda}$He) [46,47].

B. $^{10}_{\Lambda}$B

The $^{10}_{\Lambda}$B spectrum exhibits three narrow peaks in the bound region and a broader peak in the unbound region. This fine peak structure is resolved for the first time, while $^{10}_{\Lambda}$B was studied experimentally before [48,49]. All of these peaks have configurations of a Λ hyperon in the s_Λ orbit coupled

TABLE IV. Fitting results for $^{12}_{\Lambda}$C. The quoted errors are statistical.

Peaks	$M_{HY}-M_A$ (MeV)	Errors (MeV)	B_Λ (MeV)	FWHM (MeV)	σ_{2-14° (μb)
1	184.0	(fixed)	10.8	1.9±0.1	0.69±0.04
2	186.6	±0.2	8.2	1.9±0.1	0.17±0.02
3	190.9	±0.5	3.9	3.5±0.9	0.19±0.02
4	194.7	±0.2	-0.1	2.6±0.2	0.88±0.06

with a core nucleus (^{9}B). The three excited peaks are related to the excited states of the ^{9}B core at 2.4 ($5/2^-$), 7.1 ($7/2^-$), and 11.5 ($7/2^-$) MeV on the basis of the weak coupling approximation.

The spectrum was fitted with four Gaussians and a second-order polynomial representing the continuum part. The width of the Gaussians was fixed to be the estimated energy resolution, except for the fourth peak since it is wider than the energy resolution. The fitting results are shown in Table V. The obtained excitation energies (2.6, 6.3, and 9.6 MeV) are slightly shifted from the three excitation energies of ^{9}B.

A $^{10}_{\Lambda}$B spectrum was recently calculated by a configuration-mixing shell model [23,24]. The calculation showed a similar four-peak structure. Although it is for a different scattering angle, the spectrum shape will not be changed so much because of the large momentum transfer.

C. $^{28}_{\Lambda}$Si

The $^{28}_{\Lambda}$Si spectrum exhibits three clear peaks at $B_\Lambda=17$, 12, and 8 MeV in the bound region and a broad peak at $B_\Lambda=-1$ MeV in the unbound region. As argued in the BNL experiment [16,17], the three peaks at $B_\Lambda=17$, 8, and -1 MeV correspond to the configurations of $[0d_{5/2}^{-1},s_\Lambda]$, $[0d_{5/2}^{-1},p_\Lambda]$, and $[0d_{5/2}^{-1},d_\Lambda]$, respectively.

Similarly, the spectrum was fitted with five Gaussians and a second-order polynomial representing the continuum part. The Gaussian width of the ground state peak was set to be the estimated energy resolution. The strength around $B_\Lambda=6$–3 MeV (No. 4) was represented by a Gaussians although it is not a clear peak. The fitting results are shown in Table VI.

There was a calculation for $^{28}_{\Lambda}$Si by a configuration-mixing shell model, where nuclear core wave functions were treated in a full $[0d_{5/2}^{-1},1s_{1/2}^{-1},0d_{3/2}^{-1}]$ model space [50]. The observed three major peaks were reproduced by the calculation. It is interesting that the observed No. 2 strength is not sufficiently explained by the calculation. Similar strength was observed in the BNL $^{28}_{\Lambda}$Si spectrum [17].

TABLE V. Fitting results for $^{10}_{\Lambda}$B. The quoted errors are statistical.

Peaks	$M_{HY}-M_A$ (MeV)	Errors (MeV)	B_Λ (MeV)	FWHM (MeV)	σ_{2-14° (μb)
1	176.4	±0.1	8.1	2.2 (fixed)	0.17±0.02
2	178.9	±0.2	5.6	2.2 (fixed)	0.20±0.02
3	182.6	±0.2	1.9	2.2 (fixed)	0.16±0.05
4	185.9	±0.3	-1.4	4.8±0.8	0.57±0.14

TABLE VI. Fitting results for $^{28}_{\Lambda}$Si. The quoted errors are statistical.

Peaks	$M_{HY}-M_A$ (MeV)	Errors (MeV)	B_Λ (MeV)	FWHM (MeV)	σ_{2-14° (μb)
1	176.6	±0.2	16.6	2.2 (fixed)	0.09±0.01
2	181.3	±0.4	11.9	4.4±1.0	0.10±0.04
3	186.2	±0.2	7.0	2.7±0.3	0.27±0.05
4	189.0	±0.2	4.3	1.4±0.4	0.07±0.04
5	194.3	±0.8	-1.0	6.5±1.1	0.51±0.16

D. $^{89}_{\Lambda}$Y, $^{139}_{\Lambda}$La, and $^{208}_{\Lambda}$Pb

The $^{89}_{\Lambda}$Y spectrum shows characteristic peak structure. The present spectrum shape looks consistent with the one reported by the previous BNL experiment [17]. As discussed in the BNL paper, this peak structure reflects Λ-shell structure owing to the selectivity of the (π^+,K^+) reaction. Similarly, the $^{139}_{\Lambda}$La and $^{208}_{\Lambda}$Pb spectra show characteristic peak structure, which is expected to reflect Λ shell structure. Major peaks plausibly correspond to angular momentum stretched states with $g_{9/2}^{-1}$, $h_{11/2}^{-1}$, and $i_{13/2}^{-1}$ neutron holes for $^{89}_{\Lambda}$Y, $^{139}_{\Lambda}$La, and $^{208}_{\Lambda}$Pb, respectively. By referring to calculations with a simple Woods-Saxon potential [potential depth $V_0=30$ MeV, radius $r=1.1(A-1)^{1/3}$ fm, diffuseness $a=0.6$ fm] [14], those peaks are assigned to s_Λ, p_Λ, etc.

Figure 11 shows the deeply bound regions of the spectra in close-up. Since the background level is sufficiently low in the case of $^{89}_{\Lambda}$Y, the s_Λ peak can be clearly identified. Although the background levels are more conspicuous in the case of $^{139}_{\Lambda}$La and $^{208}_{\Lambda}$Pb, the observed small peaks are assumed to be the s_Λ states.

The observed spectra were found to be significantly smoother than theoretical calculations [13,14,51]. The spectrum should be sharper with the present resolution of about 2 MeV. The widths of excited states themselves are expected to be quite narrow [14,19,20]. Submajor neutron-hole series strengths such as $f_{5/2}^{-1}$, $g_{7/2}^{-1}$, and $h_{9/2}^{-1}$ for $^{89}_{\Lambda}$Y, $^{139}_{\Lambda}$La, and $^{208}_{\Lambda}$Pb, respectively, are placed between the major series peaks. Therefore, a possible reason for the smoothness may be that the nonmajor series are more important than expected.

TABLE VII. Fitting results for $^{89}_{\Lambda}$Y, $^{139}_{\Lambda}$La, and $^{208}_{\Lambda}$Pb. The quoted errors are statistical.

Spectra	Peaks	$M_{HY}-M_A$ (MeV)	Errors (MeV)	FWHM (MeV)	σ_{2-14° (μb)
$^{89}_{\Lambda}$Y	s_Λ	165.7	±0.5	2.3 (fixed)	0.04±0.01
	p_Λ	171.6	±0.3	2.3 (fixed)	0.13±0.04
$^{139}_{\Lambda}$La	s_Λ	162.0	±1.0	2.4 (fixed)	0.02±0.01
	p_Λ	165.8	±0.4	2.4 (fixed)	0.08±0.03
$^{208}_{\Lambda}$Pb	s_Λ	158.6	±0.5	2.3 (fixed)	0.02±0.01
	p_Λ	163.8	±0.7	2.3 (fixed)	0.07±0.04

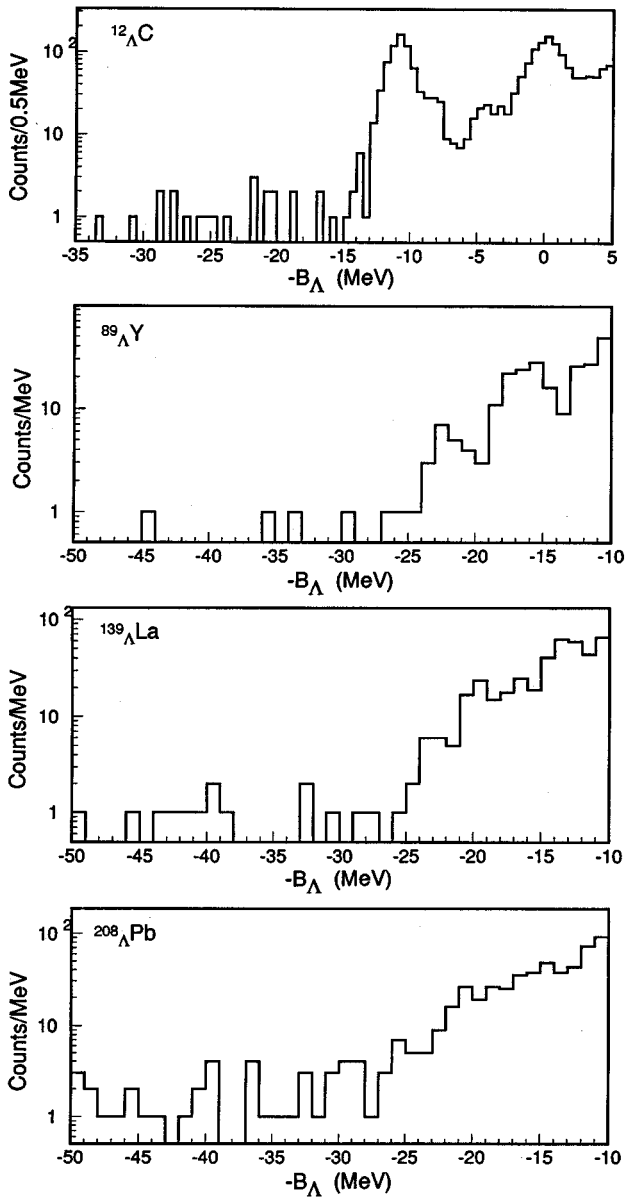

FIG. 11. Deeply bound region of the $^{12}_{\Lambda}$C, $^{89}_{\Lambda}$Y, $^{139}_{\Lambda}$La, and $^{208}_{\Lambda}$Pb spectra.

For guides to the eye and in order to obtain the binding energy of observed major peaks, fitting functions are defined as follows and shown in the spectra. In order to avoid many assumptions which are not necessarilly justified from a physics point of view, simple superpositions of Gaussians are used. The Gaussian widths are fixed to be the estimated energy resolution only for the s_Λ peaks. The fitting results are shown in Table VII. It should be noted that the results depend on these simplified assumptions about the fitting functions.

TABLE VIII. Obtained binding energies of the major Λ shell orbits. The quoted errors are statistical.

	s_Λ	p_Λ	s_Λ [17]
$^{10}_{\Lambda}$B	8.1±0.1		
$^{12}_{\Lambda}$C	10.8 (fixed)	-0.1±0.2	10.75±0.10
$^{28}_{\Lambda}$Si	16.6±0.2	7.0±0.2	16.00±0.29
$^{89}_{\Lambda}$Y	22.0±0.5	16.1±0.3	22.12±1.56
$^{139}_{\Lambda}$La	23.8±1.0	20.1±0.4	
$^{208}_{\Lambda}$Pb	26.5±0.5	21.3±0.7	

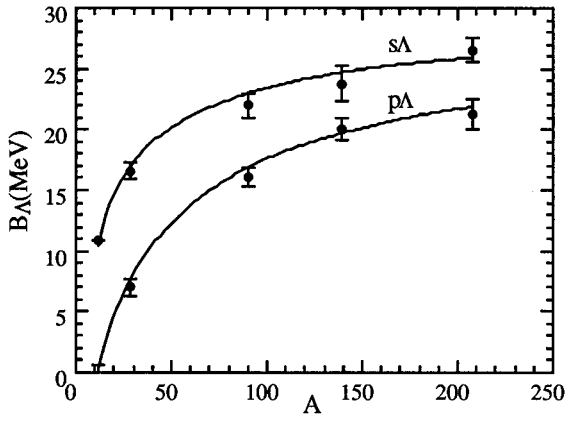

FIG. 12. Obtained binding energies of the major Λ shell orbits as a function of the mass number. Calculations with a Woods-Saxon potential [14] are shown by solid lines.

E. Mass-number dependence of B_Λ

The obtained binding energies for Λ single-particle states are listed in Table VIII. The binding energies are plotted in Fig. 12 as a function of the mass number in comparison with calculations by a Woods-Saxon potential [14]. The mass-number dependence is well reproduced by the calculation over the whole mass-number range. The $^{139}_{\Lambda}$La and $^{208}_{\Lambda}$Pb data are the first data for those heavy hypernuclear bound states. The good correspondence indicates that the independent single-particle picture of Λ hypernuclei is a good approximation.

Beyond a simple Woods-Saxon potential, a phenomenological Λ one-body potential has been developed [52,53]. Successful agreement was attained with a potential depth of 28 MeV, an effective Λ mass of 0.8 times the Λ mass, and some density dependence [52]. There is another approach starting from effective ΛN interaction [46,54], where two-body ΛN interaction is related to a one-body Λ potential by the YNG interaction. Various ΛN interaction models were employed and discussed. Although the present new data could cause important constraint on those studies, more pre-

TABLE IX. Obtained cross sections for $^{12}_{\Lambda}$C, $^{10}_{\Lambda}$B, and $^{28}_{\Lambda}$Si in comparison with other experimental results and calculations. The quoted errors are statistical.

		$^{12}_{\Lambda}$C No. 1+No. 2	$^{10}_{\Lambda}$B No. 1	$^{28}_{\Lambda}$Si No. 1
$\sigma_{2-14^\circ}/d\Omega$	μb/sr	4.7±0.4	0.9±0.1	0.5±0.1
BNL(10°) [17]	μb/sr	10.36±0.61		2.06±0.34
KEK(3°) [18]	μb/sr	15±4		
DWIA(10°) [14]	μb/sr			4.6
CMS(10°) [55]	μb/sr	8.4	3.05	

TABLE X. Extracted cross sections for $^{89}_{\Lambda}$Y, $^{139}_{\Lambda}$La, and $^{208}_{\Lambda}$Pb in comparison with other experimental results and calculations. The present results ($\sigma_{2-14^\circ}/d\Omega$) were calculated simply by dividing σ_{2-14° by the solid angle from 2° to 14° ($d\Omega$=0.183 sr). The cross sections integrated over the bound regions are also shown. The quoted errors are statistical.

	$^{89}_{\Lambda}$Y		$^{139}_{\Lambda}$La		$^{208}_{\Lambda}$Pb	
(μb/sr)	No. 1	$B_\Lambda>0$	No. 1	$B_\Lambda>0$	No. 1	$B_\Lambda>0$
$\sigma_{2-14^\circ}/d\Omega$	0.21±0.05	9.3±0.4	0.11±0.06	13.5±0.4	0.11±0.06	14.8±0.4
BNL(10°) [17]	0.54±0.38					
DWIA(0°) [14]	1.7		1.4		0.7	
DDHF(0°) [51]	2.20	81.2	1.27	103.1	0.68	82.6

cise binding energy values must be obtained with realistic fitting functions for such detailed studies.

F. Cross section

Tables IX and X list some of the obtained cross sections in comparison with other experimental data and theoretical calculations. The present results ($\sigma_{2-14^\circ}/d\Omega$) were calculated simply by dividing σ_{2-14° by the solid angle from 2° to 14° ($d\Omega$=0.183 sr). Note that they were for different scattering angles.

VI. SUMMARY

Hypernuclear mass spectra of $^{10}_{\Lambda}$B, $^{12}_{\Lambda}$C, $^{28}_{\Lambda}$Si, $^{89}_{\Lambda}$Y, $^{139}_{\Lambda}$La, and $^{208}_{\Lambda}$Pb were measured by the (π^+,K^+) reaction with an energy resolution of typically 2 MeV (FWHM). For $^{12}_{\Lambda}$C and $^{10}_{\Lambda}$B, fine peak structure related to core-excited states were resolved for the first time. It is possible to discuss the ΛN interaction by precise comparisons with configuration mixing shell model calculations. For $^{89}_{\Lambda}$Y, $^{139}_{\Lambda}$La, and $^{208}_{\Lambda}$Pb, peak structure reflecting Λ shell structure was observed. Deeply bound states such as s_Λ and p_Λ were identified in the spectra. It is found that the observed spectra are smoother than predictions. The mass number dependence of the obtained binding energies was shown to be consistent with the independent single particle picture of Λ hypernuclei. Further discussions about each spectrum are in progress in comparison with recent theoretical calculations and will be published as separate papers.

ACKNOWLEDGMENTS

The superconducting magnet of SKS was constructed in collaboration with T. Kitami, T. Morimoto, and K. Omata of INS and with Professor. T. Shintomi, Professor Y. Doi, Y. Makida, and Y. Kondo of KEK. Intensive support by Professor. T. Yamazaki, Professor K. Nakai, Professor J. Imazato, Professor Y. Ohshima, and KEK staff is greatly appreciated. Discussions with Professor. T. Motoba, Professor K. Itonaga, Professor Y. Yamamoto, and the late Professor H. Bandō were indispensable. The present work is supported in part by the U.S.–Japan collaborative research program of the National Science Foundation, the Japan Society for Promotion of Science, and the Grant-in-Aid for Scientific Research of the Japanese Ministry of Education, Science and Culture.

[1] M. Danysz *et al.*, Philos Mag. **44**, 348 (1953).
[2] M. A. Faessler *et al.*, Phys. Lett. **46B**, 468 (1973).
[3] W. Brückner *et al.*, Phys. Lett. **55B**, 107 (1975).
[4] G. C. Bonazzola *et al.*, Phys. Rev. Lett. **34**, 683 (1975).
[5] W. Brückner *et al.*, Phys. Lett. **62B**, 481 (1976).
[6] W. Brückner *et al.*, Phys. Lett. **79B**, 157 (1978).
[7] R. Bertini *et al.*, Phys. Lett. **83B**, 306 (1979).
[8] H. Tamura, Ph.D. thesis, Univ. of Tokyo, December 1987.
[9] H. Tamura *et al.*, Phys. Rev. C **40**, 479 (1989).
[10] H. Tamura *et al.*, Phys. Rev. C **40**, 483 (1989).
[11] H. A. Thiessen, AGS proposal, 758 (1980).
[12] C. B. Dover, L. Ludeking, and G. E. Walker, Phys. Rev. C **22**, 2073 (1980).
[13] H. Bandō and T. Motoba, Prog. Theor. Phys. **76**, 1321 (1986).
[14] T. Motoba, H. Bandō, R. Wünsch, and J. Žofka, Phys. Rev. C **38**, 1322 (1988); T. Motoba, Nuovo Cimento **102A**, 345 (1989).
[15] C. Milner *et al.*, Phys. Rev. Lett. **54**, 1237 (1985).
[16] R. E. Chrien, Nucl. Phys. **A478**, 705c (1988).
[17] P. H. Pile *et al.*, Phys. Rev. Lett. **66**, 2585 (1991).
[18] M. Akei *et al.*, Nucl. Phys. **A534**, 478 (1991).
[19] H. Bandō, T. Motoba, and Y. Yamamoto, Phys. Rev. C **31**, 265 (1985).
[20] A. Likar, M. Rosina, and B. Povh, Z. Phys. **A324**, 35 (1986).
[21] E. H. Auerbach, A. J. Baltz, C. B. Dover, A. Gal, S. H. Kahana, L. Ludeking, and D. J. Millener, Nucl. Phys. **A148**, 381 (1983).
[22] D. J. Millener, A. Gal, C. B. Dover, and R. H. Dalitz, Phys. Rev. C **31**, 499 (1985).
[23] K. Itonaga, T. Motoba, and H. Bandō, Prog. Theor. Phys. **84**, 291 (1990).
[24] K. Itonaga, T. Motoba, O. Richter, and M. Sotona, Phys. Rev. C **49**, 1045 (1994).
[25] O. Hashimoto *et al.*, Il Nuovo Cimento **102A**, 679 (1989).
[26] O. Hashimoto, *Perspectives of Meson Science*, edited by T. Yamazaki *et al.* (North-Holland, Amsterdam, 1992) p. 547.
[27] T. Shintomi *et al.*, IEEE Trans. Magn. **MAG-27**, 585 (1992).
[28] T. Shintomi *et al.*, IEEE Trans. Magn. **MAG-28**, 805 (1992).
[29] T. Fukuda *et al.*, Nucl. Instrum. Methods A **361**, 485 (1995).
[30] K. H. Tanaka *et al.*, Nucl. Phys. **A450**, 533c (1986).

[31] T. Hasegawa *et al.*, Nucl. Instrum. Methods A **342**, 383 (1994).
[32] T. K. Ohska *et al.*, IEEE Trans. Nucl. Sci. **33**, 98 (1986).
[33] S. Morinobu (private communication).
[34] J. C. Alder *et al.*, Nucl. Instrum. and Methods **160**, 93 (1979).
[35] H. Wind, CERN NP Internal Report 72-8 (1972).
[36] H. Grote, CERN/81-03 (1981), p. 136.
[37] J. Myrheim *et al.*, Nucl. Instrum. and Methods **160**, 43 (1979).
[38] R. E. Chrien *et al.*, Phys. Lett. **89B**, 31 (1979).
[39] D. H. Davis, Nucl. Phys. **A547**, 369c (1992).
[40] K. L. Brown *et al.*, CERN 74-2 (1974).
[41] C. B. Dover and G. E. Walker, Phys. Rep. **89**, 1 (1982).
[42] Z. Enchen *et al.*., Nucl. Data Sheets **44**, 463 (1985).
[43] B. Schorr, Comput. Phys. Commun. **7**, 215 (1974).
[44] R. E. Chrien, *Particles and Fields Series*, AIP Conf. Proc. No. 224 (AIP, New York, 1991), Vol. 43, p. 28.
[45] T. Hasegawa *et al.*, Phys. Rev. Lett. **74**, 224 (1995).
[46] Y. Yamamoto, A. Reuber, H. Himeno, S. Nagata, and T. Motoba, Czech. Phys. **42**, 1249 (1992).
[47] M. May *et al.*, Phys. Rev. Lett. **51**, 2085 (1983).
[48] M. Jurić *et al.*, Nucl. Phys. **B52**, 1 (1973).
[49] R. E. Chrien *et al.*, Phys. Rev. C **41**, 1062 (1990).
[50] T. Motoba, *Particles and Fields Series*, AIP Conf. Proc. No. 224 (Ref. 44), Vol. 43, p. 115.
[51] T. Motoba (private communication).
[52] D. J. Millener, C. B. Dover, and A. Gal, Phys. Rev. C **38**, 2700 (1988).
[53] Y. Yamamoto, H. Bandō, and J. Žofka, Prog. Theor. Phys. **80**, 757 (1988).
[54] Y. Yamamoto and H. Bandō, Prog. Theor. Phys. **83**, 254 (1990).
[55] T. Motoba and K. Itonaga (private communication).